Article

Doping with phosphorus reduces anion vacancy disorder in CdSeTe semiconductors enabling higher solar cell efficiency

Darius Kuciauskas [1] ✉, Marco Nardone [2], Patrik Ščajev [3], Chun-Sheng Jiang[4], Dingyuan Lu[5] & Rouin Farshchi[5]

Doping is used in many pn junction devices, such as polycrystalline solar cells, to increase the strength of the junction field to assist charge carrier collection and thus partially mitigate nonradiative recombination losses. We demonstrate a different doping characteristic for inorganic solar cells: using dopants to reduce charge carrier trapping and electronic band tails. Alloying CdTe with Se to form CdSeTe semiconductor reduced recombination, but CdSeTe has more complex defect states which can limit further efficiency gains due to charge carrier trapping and trap-limited mobility. Doping CdSeTe with P (but not N, As, or Sb in this study) reduces band tails (Urbach energies) and lessens the impact of the near valence band trap states, with ambipolar mobilities improving to >50 $cm^2V^{-1}s^{-1}$, fill factor increasing from 76% to 79%, and efficiencies increasing by 0.9% absolute. Simulations are used to show how such defect reduction improves performance in the radiative limit.

The increase in CdTe solar cell efficiency from 22.1% (2015) to 23.1% (2024) is attributed to improvement in open-circuit voltage (V_{OC})[1,2], which now exceeds 900 mV in polycrystalline devices[3]. Single crystal CdTe solar cells reached $V_{OC} > 1$ V with both p-type[4] and n-type[5] doping. It was proposed that smaller bandgap and recombination are the primary reasons for lower V_{OC} in polycrystalline CdSeTe[6] and it was suggested that contact selectivity can limit voltage[7]. Landmark studies guided focus on recombination[6,8,9] and advanced contacts[7,10–12]; approaches also used for perovskite (in 2015–25 small area cell efficiency increased from 20.1% to 27.0%) and silicon photovoltaics (in 2015–23 efficiency increased from 25.1% to 27.3%)[1].

We recently showed that (unlike for perovskites and silicon) electronic disorder can have a large effect on CdSeTe solar cells[13,14]. Disorder can lead to carrier trapping[14], reduce mobility[13], and can create band tails[15,16], with cumulative impacts comparable or larger than that for recombination or contact selectivity. This makes it imperative to control electronic defects in CdSeTe, including band tails[13,17,18], electrostatic potential fluctuations[14–16], and point defects[19–21].

Radiative emission spectra measured with photoluminescence (PL)[13,14,17,18,22,23] or cathodoluminescence[24] indicate complex sub-bandgap defect states, and such measurements can be used as contactless optical probes of electronic disorder. Complex CdSeTe emission spectra also require critical evaluation of thermodynamic solar cell metrics typically derived from PL−implied and radiative voltages, iV_{OC} and $V_{OC,rad}$[25]. Thus, defect characterization is also essential for material and device metrology[18,25,26].

Unlike perovskites or Cu(In,Ga)Se$_2$, high-efficiency Cd(Se)Te solar cells are intentionally doped[27]. Transition from cation-site doping with Cu to anion-site doping with As increased efficiency[6] and reliability[28] but created electrostatic potential fluctuations even in binary CdTe (no Se) absorbers[16]. Such fluctuations can impact many characteristics, from temperature coefficients[15] to voltage entitlement[15,16]. In addition to As[3,6], other group-V dopants were investigated, including Sb[29], P[2,4,30], and Bi[31]. Modeling predicted improvements with increased hole density[32] and efforts were applied to increase dopant activation in polycrystalline devices[6,15] and in

[1]Chemistry and Nanoscience Center, National Renewable Energy Laboratory, Golden, CO, USA. [2]Department of Physics, Bowling Green State University, Bowling Green, OH, USA. [3]Institute of Photonics and Nanotechnology, Faculty of Physics, Vilnius University, Vilnius, Lithuania. [4]Materials Science Center, National Renewable Energy Laboratory, Golden, CO, USA. [5]California Technology Center, First Solar, Santa Clara, California, CA, USA. ✉e-mail: Darius.Kuciauskas@nrel.gov

single crystals[33]. It was found that dopants improve performance even when carrier density introduced by doping[31] does not exceed background carrier density[17], suggesting that additional effects, such as grain growth, halide incorporation, and others, might be important. Correlation between dopant activation and performance is complex, and voltage appears to saturate at ≈900 mV, ≥200 mV below the detailed balance limit[15]. Clearly, doping impact in CdSeTe is more complex than space charge field control to enable faster minority carrier collection[32].

Here, we report electronic property analysis for polycrystalline CdSeTe doped with N, P, As, and Sb. As and P are used in the record efficiency solar cells[1–3], while Sb and N enable comparison where dopant covalent radii are smaller (N, radius 70 pm) and larger (Sb, 140 pm) in comparison to As (120 pm) and P (106 pm). We differentiate dopant interactions with hole trap states and dopant-induced changes in the electronic band tails. Doping with As increases band tails[13–16] and reduces mobility to $\mu < 1$ cm^{2}V^{-1}s^{-1} due to carrier scattering and/or trapping[13]. Doping with P improves both aspects: it reduces band tails (in comparison to As) and decreases trap defect density. Reduction in trapping with P-doping is shown even in comparison to CdSeTe without intentional doping[14,17,18,23]. Phosphorus-doped CdSeTe reaches the radiative recombination regime at low temperatures, to our knowledge the first such result for polycrystalline semiconductors. Our results reveal a different approach for improving device performance– using dopants to control not only the space charge field of the pn junction, but also electronic defect states.

Using device simulations, we consider CdSeTe solar cells with large electronic disorder (no intentional doping, N, As, and Sb doping) and with reduced electronic disorder (P doping). We show that As-doped solar cells with low hole mobility, Urbach energies $E_U \approx 30$ meV, and hole density $p \approx 10^{16}$ cm^{-3} have reached their limiting efficiency of ≈23%[13], while P-doped solar cells with $E_u \approx 20$ meV, comparable doping, and charge carrier mobility ≥50 cm^2/(Vs) can reach 25%; a long-sought target[27]. These semiconductor characteristics (doping, mobility, Urbach energy) are demonstrated in P-doped samples, indicating that the next steps are integration of such absorbers to advanced device architectures.

As proof-of-principle for approaches described in this paper, we demonstrate increase in fill factor (FF, from 76.2% to 79.2%), voltage (from 836 mV to 852 mV), and efficiency (from 19.3% to 20.2%) when P-doped heterostructures were completed to devices.

Results and discussion
Samples and methodology
Figure 1 illustrates heterostructures with graded Se composition fabricated by vapor transport deposition (VTD) of CdSe and CdTe on TCO (transparent conductive oxide) substrates and doped with N, As, P, and Sb (see Methods)[3,6,15,28,30]. Table 1 summarizes electro-optical (EO) properties, where column titles indicate dopant and chlorine heat treatment (CHT) time when this time was varied (15 min. or 45 min., see Methods).

Radiative emission spectra for our samples are similar to corresponding data for CdSeTe fabricated using close-space sublimation with controllable CdSe to CdTe ratios[18], co-evaporation of CdSe and CdTe[22], deep pocket sublimation from a ternary source followed by annealing in Se and Cd$_3$As$_2$ vapor[23], and evaporation from a ternary CdSeTe[17,24]. Substrates used in earlier studies include Corning glass[22], MgZnO on TEC12 glass[24], and Al$_2$O$_3$ on TEC12 glass[17]. Arsenic dopant incorporation in-situ (during absorber growth) and ex-situ (after absorber deposition) resulted in similar defect PL[14]. This comparison suggests that defects with complex emission signatures are intrinsic to CdSeTe or are due to the most common impurities, such as O and/or Cl. It is likely that defects analyzed here impact performance of many if not all polycrystalline CdSeTe solar cells.

Electronic defects in CdSeTe without intentional doping
First, we analyze CdSeTe without intentional doping. Emission peak at 298 K has maximum at 1.397 eV (Fig. 2a) and absorptance $a(E)$ calculated from this data is described by the Urbach energy $E_u = 14.4 \pm 0.1$ meV (Table 1). Exciton emission at low temperature (E_g (4 K)) and sub-E_g emission are distinct, indicating that broad emission at 0.8–1.4 eV is due to the defect states[13,14,17,18,22–24]. Temperature dependence is shown in Fig. 2b, where D1 indicates 1.24 eV emission and D2 indicates ≈1.0 eV emission, best resolved at 250 K. D1 and D2 defect states distinctly interact with dopants (next Section).

Activation energies $E_{A,D1}$ and $E_{A,D2}$ for D1 and D2 were determined using[34]:

$$PL(T) = \frac{I_0}{1 + a_1 T^{3/2} + a_2 T^{3/2} \exp\left(-E_A/kT\right)} \tag{1}$$

Where $PL(T)$ is PL intensity at temperature T, I_0, a_1, a_2 are constants, and k is Boltzmann's constant. Such quenching models apply to both thermally activated and tunneling multi-phonon nonradiative recombination, as analyzed next. Integration ranges 1.23–1.26 eV (for $E_{A,D1}$) and 0.78–1.1 eV (for $E_{A,D2}$) were used for all samples, best resolved for Sb-doping (next Section). Figure 2c shows that without doping $E_{A,D1} = 100 \pm 10$ meV and $E_{A,D2} = 130 \pm 20$ meV. While defect emissions are well-below the bandgap, such relatively shallow defects can allow carrier detrapping, potentially impacting charge transport.

Figure 2d illustrates configuration energy diagram (which accounts for relaxation in the excited states), consistent with earlier results for CdSeTe[13], ZnSeTe[35], CdSe[36], and first-principles models for CdSe[20] and CdSeTe[19,21]. D1 and D2 defect states can be related to anion vacancies[19,20,36], interstitials[19], or common impurities, such as oxygen[36]. D1 and D2 can be two configurations of the same defect states, or they can be distinct defects. In binary CdSe, carrier traps with D1 emission signatures were attributed to selenium vacancies[37].

As shown in Fig. S1, inhomogeneous spectral broadening at <50 K is $\Gamma_0 = 276 \pm 4$ meV. Spectral broadening is high (e.g., $\Gamma_0 = 19 - 32$ meV for hybrid lead halide perovskites[38], $\Gamma_0 = 6.0 - 6.5$ meV for ZnSe and Zn$_{0.56}$Cd$_{0.44}$Se[39], and $\Gamma_0 = 2.3–13.4$ meV for Cd$_x$Zn$_{1-x}$Se[40]) due to electronic disorder in CdSeTe. Similar electronic disorder ($\Gamma_0 > 75$ meV) was observed in polycrystalline CdSeTe fabricated by evaporation[17] and close space sublimation[14].

To learn about carrier lifetimes and defect capture and emission rates, Fig. 2e, f shows time resolved PL (TRPL) decays at different temperatures, emission energies, and time scales. Data
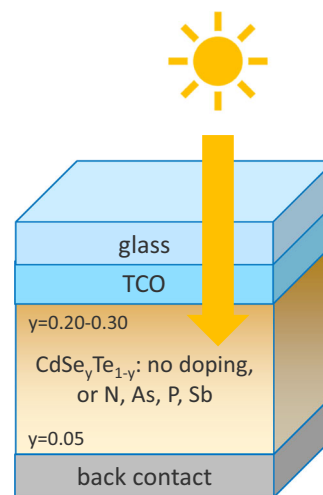

Fig. 1 | CdSeTe heterostructures used in this study. Absorbers were graded and doped as shown in the figure.

Table 1 | Electro-optical characteristics for undoped and doped (as indicated in column headings) CdSeTe heterostructures

	no doping	N	As−15	As−45	P−15	P−45	Sb
E_g, eV	1.397	1.395	1.378	1.411	1.379	1.399	
E_u, meV	14.4	16.1	25.6	24.5	21.1	20.1	
PLQY	4.1E-5	1.7E-5	5.8E-5	1.8E-6	1.2E-5	2.3E-6	3.0E-6
Stokes shift, meV	0	4	27	51	20	21	
$E_{A,D1}/E_{A,D2}$, meV	100/130	140	190/215	90	70/85	90	10/420
Γ_O, meV	276	181	344	202	132	182	
DAP shift, meV	32.8	77.7	66.4	46.4	29.3	113.3	25.6
$\tau_{2,TRPL}$, 298 K, ns	24	45	420	78	125	45	480
$\tau_{2,TRPL}$, 4-50 K, ns	4200	5600	8500	5000	160	175-400	>3000

E_g – from absorptance derivative, E_u – from fitting $a(E)$ below the bandgap to $a(E) \propto \exp((E-E_O)/E_u)$, where E is energy and E_O is a constant, PLQY – PL emission quantum yield, Stokes shift – between E_g and PL emission maximum at 298 K, $E_{A,D1}/E_{A,D2}$ – defect activation energies, Γ_O – inhomogeneous spectral broadening measured as FWHM for D1 emission at <50 K, DAP shift – injection-dependent donor-acceptor pair emission shift at 4 K, $\tau_{2,TRPL}$ – lifetime from single exponential fit to the TRPL decay.
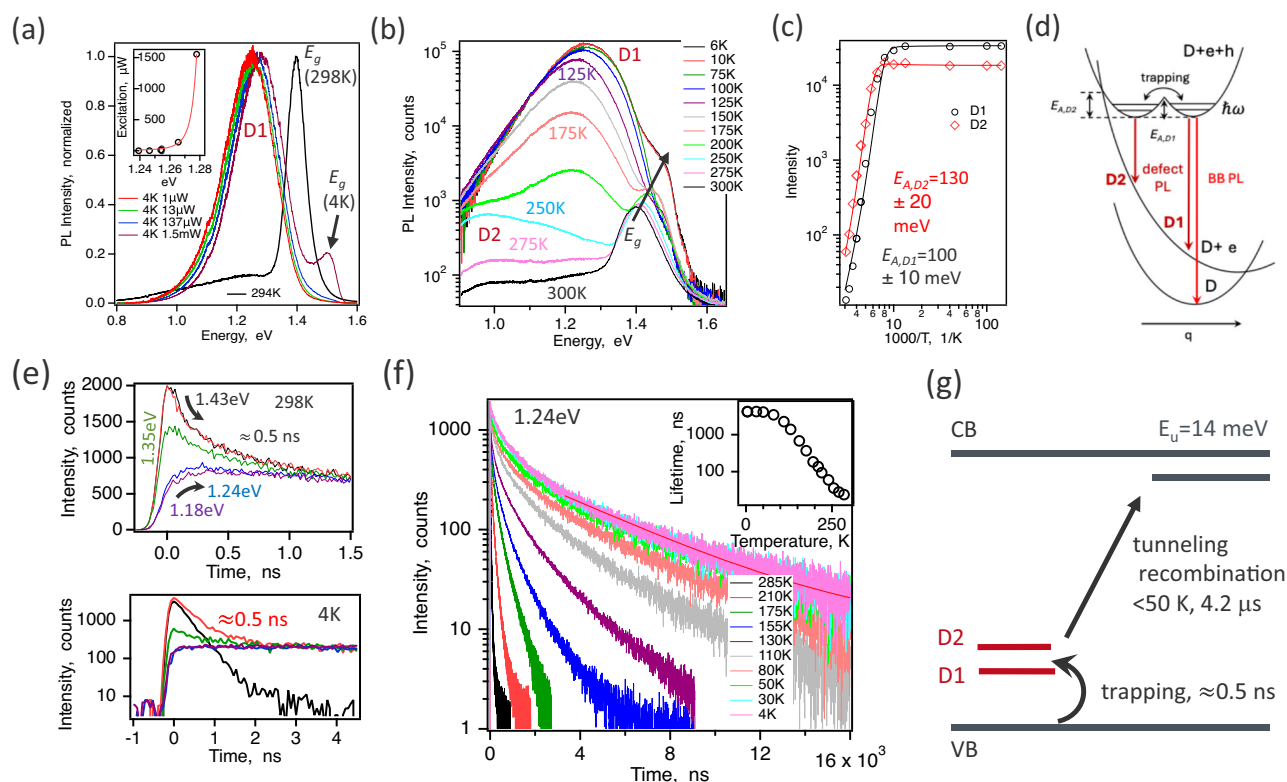

Fig. 2 | Electronic defects in undoped CdSeTe. a PL emission spectra at 298 K (black) and at 4 K. Inset shows D1 peak shift with injection. **b** Temperature-dependent PL emission spectra. **c** Analysis to determine activation energies $E_{A,D1}$ and $E_{A,D2}$; solid lines are fits to Eq. (1). **d** Configuration energy diagram for excited states (D + e + h and D + e) and the ground state (D). Red arrows indicate PL emission bands, $\hbar\omega$ is phonon energy, q is configuration coordinate. **e** TRPL decays at emission energies indicated in the legend. **f** Temperature-dependent TRPL decays measured at 1.24 eV. Inset shows lifetimes determined using single exponential fits to the decay tails, fit at 4 K is shown. **g** Band diagram summarizing results in this Figure.

clearly indicates trapping, where trap emission at 1.18–1.24 eV increases with the same rate as bandgap PL quenching ($k_{trapping} = (\tau_{trapping})^{-1} = (0.5 \text{ ns})^{-1} = 2 \times 10^9 \text{ s}^{-1}$). Since TRPL is measured at low injection, trapping dynamics is due to minority carriers. McGott et al. showed that CdSeTe has *n*-type background carrier density[17], which is also known for CdSe[20]. Thus, minority carriers in samples without doping are holes, and defects D1 and D2 with picosecond-time-scale carrier capture are hole traps close to the valence band (VB). Doping type changes with group-V doping[6,27,29], and defects D1/D2 near VB become majority carrier traps.

Heterostructures are grown on TCOs and have pn junction space charge fields, requiring numerical modeling of TRPL data to infer minority carrier lifetimes τ_B[41]. According to modeling for similar dopant density, the slower component of the TRPL decay is a good approximation for τ_B[41]. To estimate τ_B we fit the slower component of the TRPL decay $\tau_{2,TRPL}$ corresponding to ≈10% of the total amplitude. Figure 2f shows such fit for the 4 K data, and the inset indicates that $\tau_{2,TRPL}$ increases 175 times, from 24 ns at 285 K to 4.2 ± 0.5 μs at 4−50 K. Such strong temperature dependence is not consistent with Shockley-Read-Hall (SRH) recombination, where expected temperature dependence is $\propto T^{-0.5}$[42,43], and SRH lifetimes are expected to increase only 3 to 8 times in this temperature range. Microsecond lifetimes that are temperature-independent <50 K indicate tunneling recombination[14], which is attributed to electronic disorder in CdSeTe.

As shown in Fig. S2, applying the tunneling rate model[44] to low-temperature TRPL data implies defect density $(1-2) \times 10^{18} \text{ cm}^{-3}$.

Majority and minority carrier localization to the defect states is required for tunneling recombination[44]. Activation energies for defects near VB were already determined. To estimate activation energy for defects near the conduction band (CB), we analyze blue shift (to higher energy) with injection in PL spectra, Fig. 2a. This shift (of +32.8 meV) is a signature of donor-acceptor-pair (DAP) emission[44], and it indicates the binding energy for the shallower impurity[45]. We use DAP shift as an estimate for the compensating donor binding energy, $E_D \approx 33$ meV. Compensation due to such defects leads to $E_u = 14.4$ meV for undoped heterostructures.

Figure 2g summarizes all data in a band diagram. As shown next, the defect model for doped CdTe remains essentially the same. Doping, however, modifies defect properties, and with P-doping defect impact is reduced, transitioning from DAP tunneling to radiative recombination thus overcoming trapping limitations.

Band tails, compensating defects, and carrier traps in doped CdSeTe

Figure S3 shows that PL emission for doped CdSeTe becomes asymmetric and broader, which is also evident in the absorptance spectra. Urbach energies are (Table 1): $E_U = 14.1 \pm 0.1$ meV without doping, $E_U = 16.1 \pm 0.1$ meV for N-doping, $E_U = 20.1–21.1$ meV for P-doping, and $E_U = 24.5–25.6$ meV for As-doping. In comparison to single crystal CdTe ($E_U \approx 8$ meV)[14], silicon ($E_U \approx 9$ meV)[46], perovskites ($E_U \approx 13$ meV[47], $E_U \approx 18$ meV for larger bandgaps)[48], and Cu(In,Ga)Se$_2$ ($E_U \geq 15$ meV)[47], E_U values in doped CdSeTe are higher.

Spectral broadening in doped semiconductors with low dopant activation is usually attributed to compensation[15,16]. As explained earlier and shown in Fig. 3a, activation energies of compensating defects were estimated from DAP spectral shifts.

In addition, potential fluctuations are commonly evaluated for disordered semiconductors[49]. Since the CdSe$_y$Te$_{1-y}$ composition y is close to the E_g bowing minimum[50], amplitude of bandgap fluctuations is low[15]. Electrostatic potential fluctuation amplitude, γ, can be estimated using analytical models[51]. Using dopant density measured with SIMS (secondary ion mass spectrometry, Fig. S4a and Fig. S14) and carrier density measured with CV (capacitance voltage, Fig. S4b), $\gamma = 111–255$ meV for As-doping, $\gamma = 92–189$ meV for P-doping, and $\gamma = 37–89$ meV for N-doping (Table S1).

Finally, Stokes shifts between absorption and emission spectra are also listed in Table 1. These four sets of metrics (E_u, energy of compensating defects, γ, and Stokes shift) can correlate with radiative voltage $V_{oc,rad}$[15,16,18,46,47]. However, majority carrier traps (D1/D2) are the most critical CdSeTe defects because such traps can reduce mobility and thus FF of solar cells[13,14,25].

Activation energies $E_{A,D1}/E_{A,D2}$ for traps D1/D2 were determined from PL(temperature) data in Fig. 3c as shown in Fig. S5 and illustrated in band diagrams in Fig. 3b. In comparison to CdSeTe without doping, As-45, P-45, and P-15 heterostructures have shallower traps and N, As-15, and Sb-doped heterostructures have deeper traps. D1 and D2 activation energies are within 30 meV in all cases except Sb, where $E_{A,D1}$ is low and $E_{A,D2}$ has the highest value. Using P-doping decreases $E_{A,D1}/E_{A,D2}$ even in comparison to undoped CdSeTe, while band tails (compensation) increase less with P than with As. In addition, inhomogeneous broadening (Fig. S1) is the lowest for P-doped heterostructures.

As is the case for undoped CdSeTe, first principles studies suggest possible defects in group-V doped CdSeTe[21,52,53]. Such defects can include Cd$_i$ + As$_{Te}$[21] and AX centers[52,53]. It was suggested that P can be a more efficient dopant than As due to reduced compensation[21], in agreement with lower E_U values for P-doping. Experimental defect identification is challenging because of broadening and potential overlap of spectroscopic signatures.

Scanning Spreading Resistance Microscopy (SSRM) data in Fig. 4 shows nm-to-μm-scale variation of electrical resistance taken at the delaminated front Cd(Se)Te interface, where the measured resistance is dominated by the local resistivity below the AFM probe[30]. The resistance of P-45, As-45, and Sb-45 samples show similar non-uniformity with relative standard deviation Rq/R ≈ 0.5 and amplitude variation of one order of magnitude. For the N-45, P-15, and As-15 samples the nonuniformity is larger with Rq/R > 0.75 and amplitude variation of about 3 orders of magnitude. These resistance non-uniformity trends are not consistent with the amount of the electronic disorder, illustrating that the electronic disorder did not result from the doping nonuniformity, but is attributed to defects and their complexes originating at the CdSeTe anion sublattice.

Contrasting carrier dynamics in doped CdSeTe: from tunnelling to radiative recombination

Emission spectra identified dopant-dependent defects D1/D2 and compensating centers, resulting in complex energy diagrams. We used TRPL, Light-Induced Transient Grating (LITG), and pump-probe (PP) measurements to analyze how defects impact carrier dynamics[13]. First, we consider P-45 heterostructure. Figure 5a shows TRPL decays (measured at 1.24 eV) at 285 K, 35 K, and 6 K. We used the TRPL tail fitting model[41] described earlier to determine $\tau_B \approx \tau_{2,TRPL} = 45$ ns at 285 K, 300 ns at 35 K, and 175 ns at 6 K. Increase in recombination rate $\tau_{2,TRPL}^{-1}$ between 35 K (3.3×10^6 s^{-1}) and 6 K (5.7×10^6 s^{-1}) is a reliable signature of radiative recombination[42]. A similar trend is observed for the P-15 heterostructure, Fig. S6.

As shown in Fig. 5b, rates $\tau_{2,TRPL}^{-1}$ were fit to[42,43]:

$$\frac{1}{\tau_2} = \frac{1}{\tau_{rad}} + \frac{1}{\tau_{SRH}} + \frac{1}{\tau_{act}} \propto C_{rad}T^{-1.5} + C_{SRH}T^{0.5} + C_{act}T^{0.5}\exp\left(-\frac{E_{A,TRPL}}{kT}\right) \quad (2)$$

Where τ_{rad}^{-1}, τ_{SRH}^{-1}, τ_{act}^{-1} are radiative, SRH, and activated rates, C_{rad}, C_{SRH}, and C_{act} are constants, and $E_{A,TRPL} = 80 \pm 20$ meV is activation energy (measured from the Fermi level). Analysis identifies that at 6 K radiative recombination makes the largest contribution, at 35 K radiative and SRH rates are comparable, and above 200 K activated process has the highest rate.

Minimal or no trapping with P-doping is also suggested by τ_{rad} values. The temperature dependence of the radiative constant is $B = B_o(300/T)^{3/2}$[42], where $B_O = (1–2) \times 10^{-10}$ cm^{3}s^{-1}[54]. If hole density at 6 K is $p \approx 1 \times 10^{15}$ cm^{-3}, $\tau_{rad} = 1/Bp = 15–30$ ns at 6 K. Estimated τ_{rad} is similar to $\tau_{2,TRPL}$, indicating that free carrier density at 6 K is not much lower than 10^{15} cm^{-3}.

Next, we directly measured charge carrier mobility with LITG spectroscopy, where laser excitation modulates carrier density and an optical beam diffracted from the carrier grating probes lateral diffusion and recombination. By using several grating periods, diffusion and recombination processes can be separated[13]. Figure S7 shows LITG data and analysis, and Fig. 5c shows injection-dependent ambipolar diffusivity D and mobility μ. At the lowest fluence, $D = 1.8 \pm 0.2$ cm^{2}s^{-1} corresponding to $\mu = 69 \pm 8$ cm^{2}V^{-1}s^{-1}. Because hole effective mass is ≈ 4 times higher, hole mobility $\mu_p = 35 \pm 4$ cm^{2}V^{-1}s^{-1} and electron mobility $\mu_e = 140 \pm 16$ cm^{2}V^{-1}s^{-1}, excellent values for polycrystalline semiconductors. In addition to diffusivity and mobility measurements shown in Fig. 5c, we analyzed absolute LITG diffraction intensities (Fig. S8) and found carrier effective masses consistent with literature values, further supporting increased mobility in P-doped CdSeTe.

Increase of D with injection identifies ionized impurity scattering and/or random alloy scattering as possible mechanisms limiting mobility from single-crystal values.[55] The same mechanisms lead to PL broadening (Fig. S1). Hall mobilities in As-doped single-crystal CdTe with similar dopant activation are comparable[33,56], further indicating that compensation (resulting in ionized impurity scattering) limits mobilities in P-doped heterostructure, rather than grain boundary or extended defect scattering, which would presumably differ in polycrystalline and single crystal absorbers.
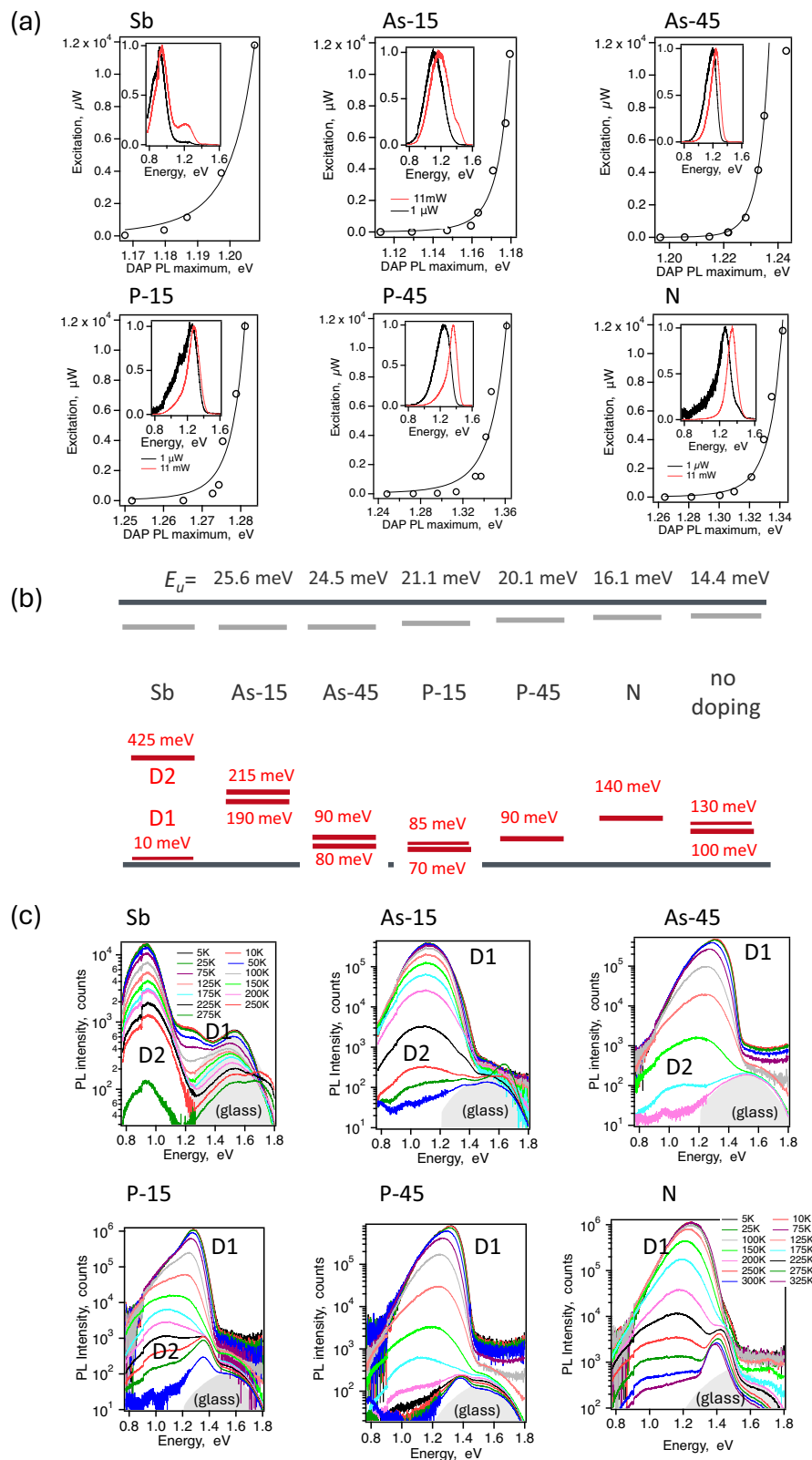
Fig. 3 | Compensation and carrier traps in doped heterostructures. a Injection-dependent donor-acceptor pair (DAP) spectral shifts at 5 K. Lines are fits to the model from ref. 45. Insets show spectra measured with the lowest (black) and the highest (red) injection. **b** Defect energy diagrams. Values are also listed in Table 1. **c** Temperature-dependent PL emission spectra used to determine D1/D2 activation energies. Excitation fluence was the same and intensities can be compared. (Gray shaded areas indicate scattering from glass substrates).
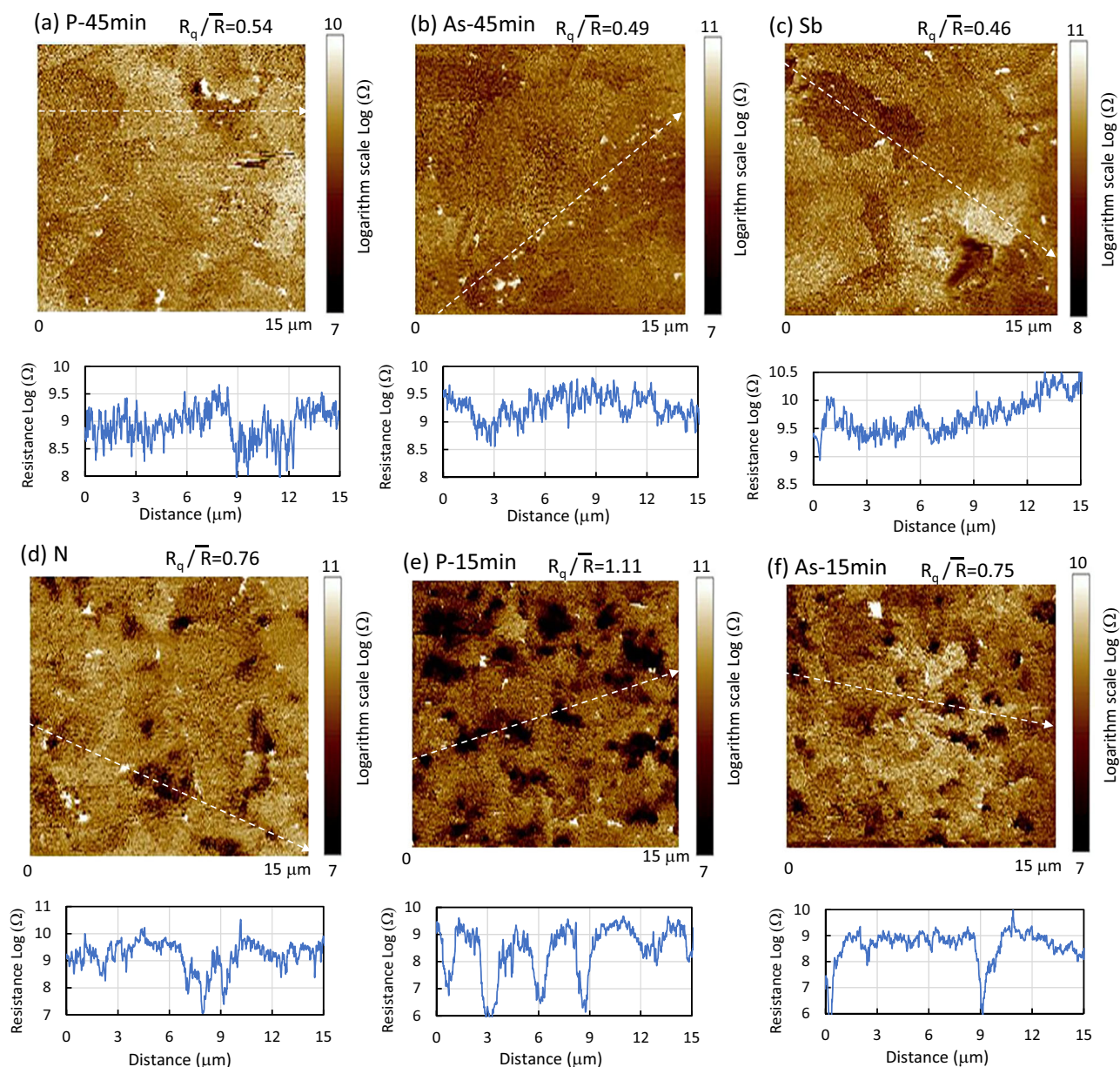
Fig. 4 | Scanning spreading resistance microscopy (SSRM) data and analysis. **a–f** SSRM images taken with positive sample bias voltage Vs = +10 V at the CdSeTe front interface for all dopants in this study, as indicated in the legends. Dashed lines indicate directions of representative resistance line profiles shown in panels below images. Resistance is shown using logarithmic scales.

While inhomogeneous broadening in CdSeTe:P is larger than that for hybrid lead halide perovskites (Γ_0 = 132 meV vs. Γ_0 = 19–32 meV[38]), mobility in CdSeTe:P is higher (35 cm^{2}V^{-1}s^{-1} vs. 0.1–2.2 cm^{2}V^{-1}s^{-1} for FAPbI$_3$[57]), indicating that scattering mechanisms in solar semiconductors need further studies.

Because LITG measurements were performed using pulsed excitation and trap occupancy might differ with continuous-wave excitation, we repeated LITG experiments with light bias, where bias light fluence was approximately 1 Sun. As shown Fig. 5c, diffusivities and mobilities with and without light bias were approximately the same.

To further show that carrier trapping is reduced with P-doping, transient absorption (TA) measurements were applied. TA probes carrier dynamics for radiative and non-radiative states, and is especially useful for monitoring states with low radiative efficiency[56]. As shown in Fig. S9, TA lifetimes are in good agreement with TRPL data.

In summary, P-doped heterostructures in this study no longer have trapping limitations as probed by TRPL lifetime temperature dependence, LITG diffusivity injection dependence with and without light bias, and TA data.

Trapping persists for other samples. Figure S10 shows temperature-dependent TRPL decays and Fig. 5d contrasts TRPL(temperature) data for all heterostructures. For As-45 and N-doping $\tau_{2,TRPL}$ = 5.0–5.6 µs and lifetimes are temperature-independent at ≤40 K, indicating trapping followed by tunneling recombination. Tunneling center density is comparable, (1–2) × 10^{18} cm^{-3} with and without doping, Fig. S2.

As-15 and Sb-doped heterostructures have the deepest traps, and as shown in Fig. S11, trapping is already impacting carrier dynamics at room temperature, with $k_{trapping} \approx (0.5 \text{ ns})^{-1} = 2 \times 10^9$ s^{-1}. For Sb-doping lifetimes of the D1 and D2 states can be differentiated from PL emission at 1.24 eV (D1) and 0.83 eV (D2).

Taken together, data indicates that using anion-site doping it is possible to change electronic disorder in CdSeTe. Defect D1 inhomogeneous broadening can range from Γ_0 = 132 meV (P-15) to 344 meV
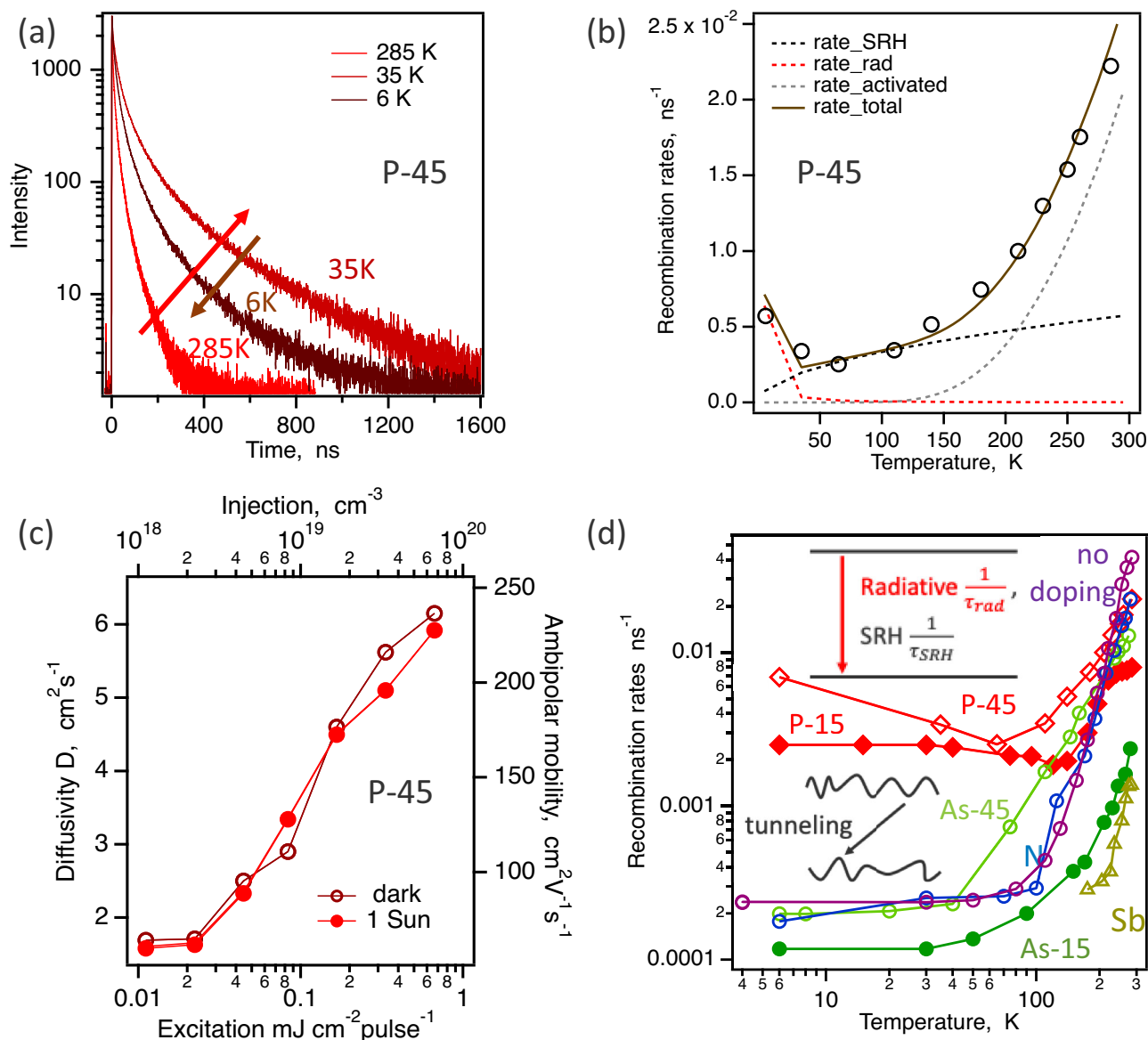
Fig. 5 | Carrier dynamics. a–c Data for P-45 heterostructure. **a** TRPL decays at 285 K (red), 35 K (dark red), and 6 K (brown). **b** Recombination rate analysis using Eq. (2). **c** Injection dependence for lateral ambipolar diffusivity and mobility, with and without light bias, when the grating period was 1.2–6.8 μm. **d** Recombination rates for all samples. Insets indicate that radiative recombination dominates with P-doping and tunneling recombination due to trapping is observed for other samples.

(As-15), hole trap activation energies can range from 70 meV (P-15) to 420 meV (Sb), carrier lifetimes can range from radiative (P-15) to limited by trapping at the room temperature (As-15, Sb). To evaluate impacts on solar cells, we included extended range of electronic characteristics to solar cell device models.

Device modeling in the radiative limit with the shallow defect states

Device modeling was conducted to quantify the effects of shallow defects and transport characteristics on device performance relative to the radiative limit. Shallow defect states can affect device performance in various ways, including (i) increasing V_{oc} when acting as dopants, (ii) reduction of mobility due to charge carrier scattering, (iii) interactions with dopant species thereby impacting the junction electric field, and (iv) creation of band tails (characterized by E_u). The latter can lead to lower V_{oc} due to a reduced recombination activation energy, but higher J_{sc} due to enhanced absorption of lower energy photons[46,58].

To capture shallow defect features, simulations were performed in the parameter space $\mu_p = 0.1$–50 cm^{2}V^{-1}s^{-1}, $N_A = 10^{14}$–10^{17} cm^{-3}, and $E_u = 0$–30 meV. The minority carrier mobility was kept fixed at 320 cm^{2}V^{-1}s^{-1}[159], while the majority carrier mobility μ_p was varied to consider the effects of hole traps (varying μ_n is explored later). E_u was used to calculate both the V_{oc} loss and the absorption coefficient, $\alpha(E)$, as described in the Supplementary Information. V_{oc} loss was captured with a reduced bandgap[46,60–62]. To simulate the radiative limit, non-radiative recombination was omitted, contacts were assumed Ohmic, and interfaces had no surface recombination or detrimental band offsets. Se grading (y in CdSe$_y$Te$_{1-y}$) as a function of depth, x, was set to an erfc(x) dependence with y = 0.3 at the SnO$_2$/Cd(Se,Te) interface and y = 0 at 1.5 μm distance from that interface[41]. E_g and electron affinity gradings were determined from the published bowing functions[50]. A list of simulation parameters is provided in the Supplementary Information and methodology is described in Methods.

Figure 6a–c shows how the efficiency varies with μ_p and doping for $E_u = 0$, 20, and 30 meV. Increased doping tends to improve
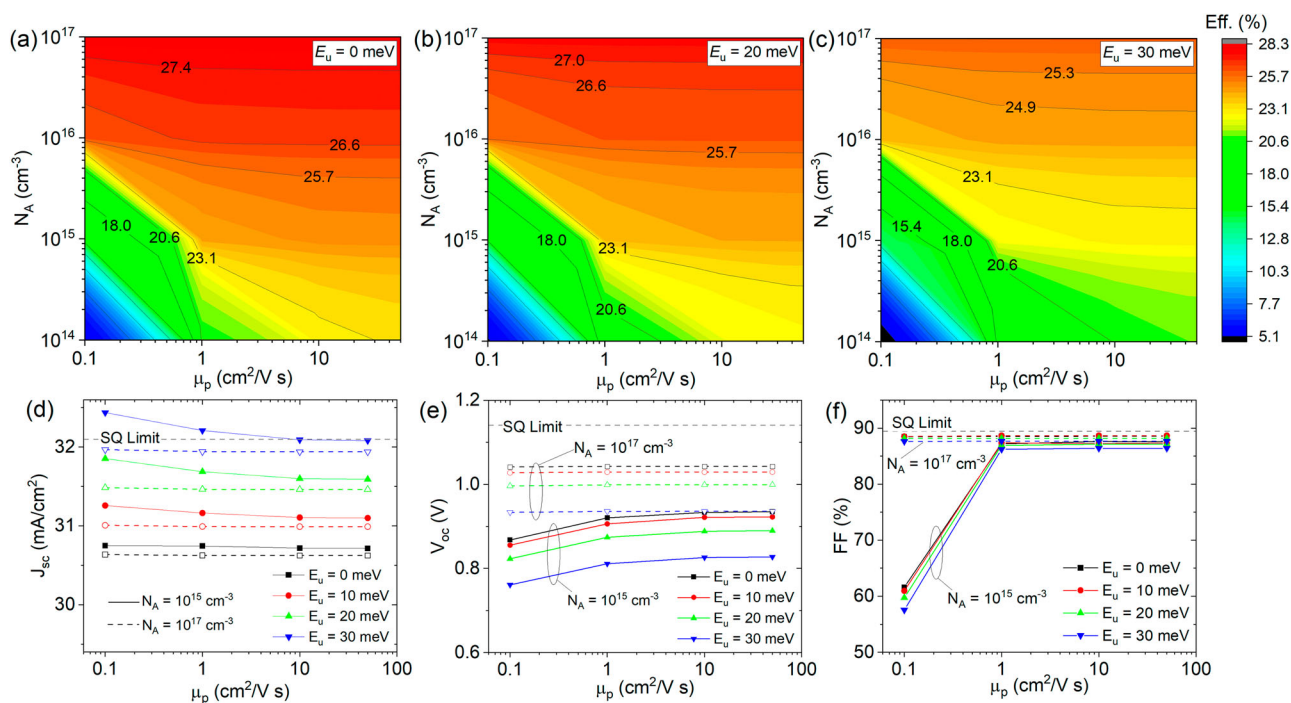
Fig. 6 | Simulated performance metrics in the radiative limit with shallow defect effects. Efficiency as a function of hole mobility (μ_p) and acceptor doping (N_A) for Urbach energies of (**a**) E_u = 0 meV, (**b**) E_u = 20 meV, and (**c**) E_u = 30 meV. Common color legend on the right. Performance metrics for (**d**) short-circuit current (J_{sc}), (**e**) open-circuit voltage (V_{oc}), and (**f**) fill factor (FF) as functions of μ_p for E_u = 0–30 meV and doping levels of N_A = 10^{15} cm^{-3} (solid lines) and N_A = 10^{17} cm^{-3} (dashed lines). The SQ limit for each metric is the horizontal dashed line.

efficiency, especially when mobility is low. For all E_u values, hole mobility $\mu_p \leq 1$ cm^{2}V^{-1}s^{-1} is very detrimental to device performance due to FF and V_{oc} loss when $N_A < 5 \times 10^{16}$ cm^{-3}. Band tails reduce the maximum radiative efficiency, with values of 28.3%, 27.7%, and 26.2% when E_u = 0, 20, and 30 meV, respectively. The efficiency for E_u = 10 meV (not shown) is nearly identical to that of E_u = 0 meV, indicating that small tails of $E_u \approx$ 10–20 meV can be tolerated. There is significant qualitative change near $N_A = 10^{16}$ cm^{-3}. Hence, Fig. 6d–f shows the performance metrics for $N_A = 10^{15}$ cm^{-3} and $N_A = 10^{17}$ cm^{-3} as functions of mobility and E_u. All metrics are independent of mobility at $N_A = 10^{17}$ cm^{-3}. At $N_A = 10^{15}$ cm^{-3}, however, the negative impact of low mobility on FF is evident, in addition to some V_{oc} loss. At higher doping, there is a slight loss in J_{sc} due to the decreased extent of the junction electric field. That loss is more than compensated for by increases in V_{oc} and FF with doping. Oddly, J_{sc} increases slightly at low doping as Urbach energy increases and mobility decreases. At low doping and low mobility, injected charge (greater with band tails) is sufficient to reduce the net space charge in the depletion region, resulting in a larger depletion width and better carrier collection under short circuit conditions. Band tails cause a slight increase in J_{sc} while significantly reducing V_{oc} with losses of 13, 25, and 108 mV for E_u = 10, 20, and 30 meV, respectively (see Table S3).

The Shockley–Queisser (SQ) limits for each metric (assuming E_g = 1.42 eV and interpolated from ref. 63 are shown as the horizontal dashed lines in Fig. 6d–f. Without band tails (E_u = 0 meV) and at the highest doping, the best values of J_{sc} and V_{oc} are below the SQ limit by 4.7% (1.5 mA/cm^2) and 8.6% (98 mV). J_{sc} increases beyond the SQ limit when E_u = 30 meV because the detailed balance calculation assumes an abrupt absorption edge, which neglects some band-tail-induced photocurrent enhancement. Despite the device models being set to the radiative limit, the metrics fall short of the SQ values mostly due to the lack of photon recycling[64], but also because of a constant reflectivity of 2% and absorption losses in the buffer layer. For the same reasons, the highest simulated efficiency is 28.3%, while the SQ limit is 32.66%. Even higher absorber doping of 10^{18} cm^{-3} increases efficiency to 28.8% (not

shown), but surpassing 29% would require meticulous optical management.

Device results

Spectroscopy indicated potential advantages of P-doping by reducing band tails and hole traps, and device modeling benchmarked performance in the radiative limit due to such improvements. To test these predictions, we completed P- and As-doped heterostructures to solar cell devices, see Methods.

Figure 7 shows JV and EQE data for the best As- and P-doped devices selected from a set of 12 for each doping type. The inset table indicates statistics for efficiency, J_{SC}, V_{oc}, and FF. Simulated JV and EQE curves, in good correspondence with the data, are also shown in Fig. 7. The device models are the same as the idealized case in Fig. 6, except that the P-doped model assumed μ_p = 10 cm^{2}V^{-1}s^{-1} and E_u = 20 meV (Stokes shift = 20 meV). Values for the As-doped model were μ_p = 0.35 cm^{2}V^{-1}s^{-1}, E_u = 25 meV (Stokes shift = 50 meV). The low mobility for As-doped CdSeTe was previously reported[13], and E_u and Stokes shift were based on the values in Table 1. Both models assumed $N_A = 2 \times 10^{16}$ cm^{-3} (from typical CV measurements for these devices), bulk nonradiative lifetime τ_B = 2 ns (devices had similar PLQY, Table 1), and contact series resistance R_s = 0.3 Ω cm^2. Increases in V_{oc} and FF for the P-doped device are due to lower E_u and higher μ_p, respectively. As expected, J_{SC} remains approximately the same, with slightly higher current with As-doping likely due to band tail effects (see Device modeling section). The P-doped JV curve is insensitive to further increases in μ_p, so the actual value could be ≥ 10 cm^{2}V^{-1}s^{-1}. The effects of varying μ_n on the JV characteristics for this device are shown in Fig. S13. Comparison to device data suggests that $\mu_n > 100$ cm^{2}V^{-1}s^{-1}. Voltage for both models is very sensitive to τ_B. For example, increasing τ_B from 2 ns to 100 ns results in a 25.6%-efficient device with V_{oc} = 976 mV, suggesting that further improvements could be gained by reducing nonradiative recombination. The corresponding radiative limit in Fig. 7b is 26.4%. Overall, device efficiency for P-doping increases by 0.9% absolute, with 0.3% from
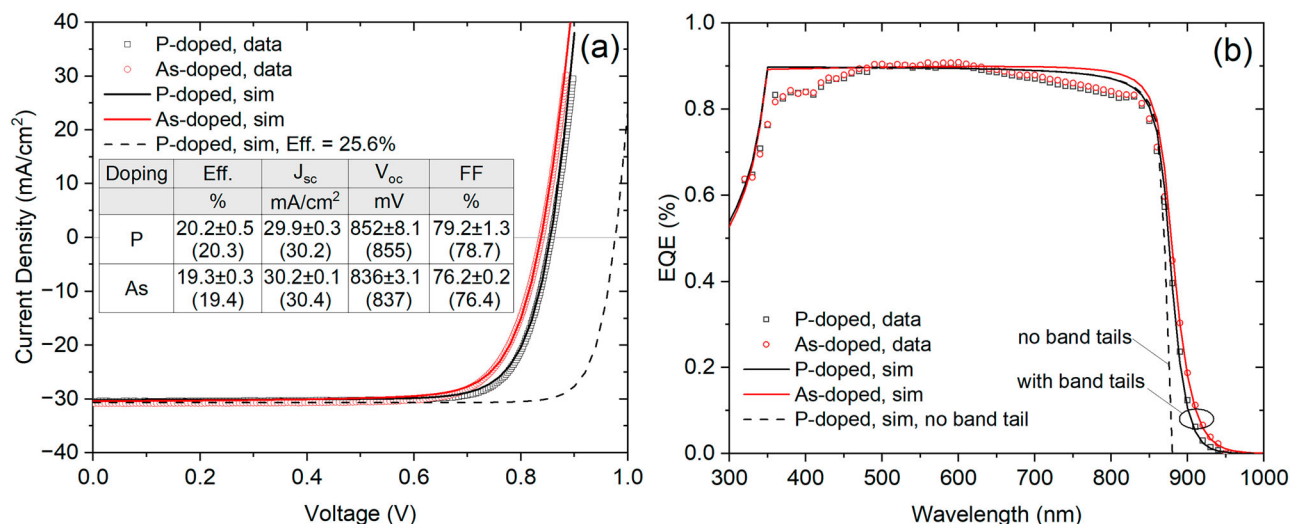
Fig. 7 | Solar cell device results and comparison with device models. a JV and (**b**) EQE data (points) for As- and P-doped devices compared to simulation results (solid curves). Performance metrics are provided in the inset table (for 12 devices) with simulation results in parenthesis. The JV curves pertain to the best devices with higher V_{oc} (lower E_u) and 0.6% from higher FF (higher μ_p). This indicates significant potential to increase CdSeTe solar cell performance with tailored defect control using dopants.

The EQE simulations in Fig. 7b account for the observed broadening at long wavelengths when band tails with E_u = 20 and 25 meV are included for P-doped and As-doped devices, respectively. Omitting band tails results in the abrupt cutoff shown by the dashed line. Discrepancies at wavelengths less than 850 nm are due to the simple optical model that does not include wavelength-dependent reflection or thin film interference effects.

efficiencies of 19.7% and 20.7% for As and P doping, respectively. **a** Increasing τ_B from 2 to 100 ns increases efficiency to 25.6% (dashed). **b** Omitting band tails in the P-doped device model results in an abrupt long wavelength EQE cutoff (dashed).

Summary

CdSeTe PV has reached over 50 GW$_{pp}$ (peak power) cumulative installations and 20 GW$_{pp}$ annual manufacturing capacity[15], making understanding of efficiency potential and limitations of this material system highly pertinent. To make progress towards this goal, we developed defect models for group-V doped CdSeTe and applied these models to state-of-the-art thin film solar cells. Defects in CdSeTe are complex, making it necessary to consider not only solar cell thermodynamics[46,47,58], but also charge transport. Mobility is a critical parameter for CdSeTe solar cells due to majority carrier (hole) trapping[13,14,25]. Complex near-E_g defects also increase band tails. Although numerous forms of disorder can cause band tails, in this case, it appears that anion disorder and, possibly, a high degree of nonuniform dopant compensation result in band tails that reduce the activation energy for electron-hole pair generation, as indicated in the EQE results. The same activation energy reduction affects recombination according to the Stoke's shift in the PL data. We hope results reported here clarify multiple impacts that doping on anion sites can have in CdSeTe solar cells, largely due to anion disorder in this semiconductor.

We show that doping polycrystalline CdSeTe with phosphorus overcomes trapping limitations and increases mobilities to values equal to those of compensated CdTe single crystals, $\mu_p \geq 50$ cm^{2}V^{-1}s^{-1}[33,55,56]. With P-doping, electronic disorder (inhomogeneous broadening, E_u, trap activation energy) is reduced, and low temperature charge carrier lifetimes reach the radiative limit. Device modeling identified that solar cells with EO characteristics demonstrated in the study have the potential to reach 25% efficiency, which would be a breakthrough for CdTe PV[27]. In addition to seeking higher radiative efficiency[6] for energies at or above absorbed photons energies and better contact selectivity[7], reducing electronic disorder becomes an important research direction for CdTe PV. Corroborating results from characterization and modeling, we demonstrate device FF increase from 76% to 79% and efficiency improvement +0.9% absolute with P-doping, which is primarily attributed to increased μ_p due to reduced trapping.

To our knowledge, this is the first demonstration of decreasing electronic disorder by doping in inorganic semiconductors. Such results were reported for conjugated organic polymers[65], which are more tunable due to conformational, structural, and other flexibility inherent in organic materials. In addition to doping, other processes could improve charge transport in CdSeTe. For example, polycrystalline CdSeTe where several high temperature anneals were used to increase crystalline grain sizes to ≥10 μm had high mobility (≈100 cm^{2}V^{-1}s^{-1}) and diffusion length (≈10 μm)[66]. Combining doping with thermal treatments might reduce passivation requirements and improve device contacts. Using additives, such as dopants, to change defect properties can also be a promising method for understanding and reducing defects in other polycrystalline semiconductors.

Methods

Fabrication of heterostructures and solar cells

Polycrystalline CdSe$_y$Te$_{1-y}$ semiconductors were grown by vapor transport deposition (VTD) of CdSe and CdTe on glass substrates coated with fluorine-doped tin oxide as the transparent conductive oxide (TCO)[3,6,15,30]. The CdSe$_y$Te$_{1-y}$ layers have graded Se content with y = 0.20–0.30 near the TCO with the bandgap $E_g \approx 1.4$ eV and y < 0.05 at the back with $E_g \approx 1.5$ eV. The analytical model for the grading profile was described[41], and it was also used in device simulations. Dopants were incorporated into the CdSeTe absorber after the VTD step, followed by a chlorine heat treatment (CHT) where annealing is carried out in the presence of CdCl$_2$ at temperatures between 400 and 500 °C, introducing Cl at levels on the order of 10^{18} cm^{-3}. During the CHT step, dopant activation occurs in addition to Se diffusion, chlorination, and grain growth[3,6,15,30]. For As- and P-doping CHT treatment times were 15 min. and 45 min., and it was 45 min. for Sb and N-doping. Samples where CdCl$_2$ treatment time was varied are identified as As-15/As-45 and P-15/P-45. P- and As-doped heterostructures were completed to devices by depositing a ZnTe layer that was capped with a metal stack[10,28].

Characterization of solar cells

Selenium grading and dopant incorporation were measured by SIMS (secondary-ion mass spectrometry) and carrier density was measured by CV (capacitance voltage). CV characteristics were measured with an Agilent E4980A impedance analyzer. Voltage was scanned from −2 to +0.5 V in 0.1 V steps in the dark, with a measurement frequency of 40 kHz. SIMS data were collected using a TOF-SIMS-5 instrument with O_2-negative profiling. Arsenic-doped samples without metal back contact, including graded-E_g and uniform-E_g compositions, were studied in ref. 13.

Current-voltage measurements were performed using a Newport Model SP94061A-SR1 solar simulator at 1 sun with sample air cooling to maintain 25 °C and scanning from −0.75 to 1.25 V at a rate of 0.93 V/s with 6.5 mV steps. Efficiency, J_{SC}, V_{OC}, and FF are summarized in Fig. 7, where uncertainties indicate standard deviations of these parameters for 12 devices.

Photoluminescence spectroscopy

Absolute PL emission spectra were measured with 1 Sun equivalent excitation $(1.98 \times 10^{22}$ photons cm^{-2}s$^{-1})$ at 632.8 nm using 300 mm spectrograph equipped with Si CCD and InGaAs array detectors[14]. Spectral response was corrected using calibration sources provided by the manufacturer (Princeton Instruments), and absolute photon numbers were obtained using reflectance standards (Lab Sphere). TRPL was measured using excitation at 640 nm (300 fs pulses, Pharos/Orpheus OPA system, Light Conversion) and time-correlated single photon counting with Si and gated InGaAs/InP detectors (Picoquant and Micro Photon Devices). For low temperature measurements closed loop He cryostats were used.

Light induced transient grating and pump probe spectroscopy

For light induced transient grating (LITG) and pump-probe (PP) spectroscopy, 10 ps excitation pulses at 527 nm were used. Probe wavelengths were 1056 nm (LITG) and 1550 nm (PP) and the measurements were performed in transmission geometry, as described earlier[13]. The LITG grating period was varied from $\Lambda = 1.2$ μm to 6.8 μm. Light bias in LITG and PP measurements utilized 532 nm continuous-wave laser and fluence of 70 mWcm^{-2}.

Scanning spreading resistance microscopy

SSRM is based on the contact mode of AFM (Bruker Dimension Icon and Nanoscope V) and set in an Ar-glovebox with a logarithm-scale amplifier (Bruker SSRM module) to measure a wide range of resistance $(10^3 - 10^{14}$ Ω)[30]. The probe (Bruker DDESP-V2) is a highly doped diamond-coated Si tip. SSRM is a two-terminal resistance measurement with a bias voltage applied to the sample (Vs), and the probe is floating-grounded. The contact resistance is suppressed sufficiently below the spreading resistance by applying a large probe/sample contact force (≈1 mN) and a large forward sample bias voltage (Vs = +10 V). For sample preparation, the front interface was delaminated by thermomechanical stressing in liquid nitrogen.

Device modeling

Device simulations were conducted using COMSOL Multiphysics® software. The Poisson and current continuity equations were solved numerically by the finite-element method. Simulations of current density versus voltage (JV) were conducted at a temperature of 298 K in the dark and at 1-sun intensity illumination with the AM1.5 G spectrum. Absorber doping density, hole mobility, and Urbach energy were independently varied for this study. Graded CdSeTe band gap, $E_g(x)$, and electron affinity were included as described in the text. Due to band-gap grading, a depth-dependent absorption coefficient was used in the CdSeTe layer, $\alpha(E, x) = A\sqrt{E - E_g(x)}$, where $A = 10^5$ cm^{-1} eV$^{-1/2}$ and $E \geq E_g(x)$ is photon energy. For cases with band tails, $\alpha(E, x)$ was convoluted with an exponential function with decay energy E_u. Further

details and parameter values, largely based on refs. 32 and 41, are provided in the Supplementary Information.

Reporting summary

Further information on research design is available in the Nature Portfolio Reporting Summary linked to this article.

References

1. https://www.nrel.gov/pv/cell-efficiency.html, accessed May 1, 2025.
2. Lu, D. et al. The role of dopants, recombination, and bandtails on the road to 25% and beyond in Cd(Se,Te) solar cells, in preparation.
3. Mallick, R. et al. Arsenic-doped CdSeTe solar cells achieve world record 22.3% efficiency. *IEEE J. Photovolt.* **13**, 510–515 (2023).
4. Burst, J. M. et al. CdTe solar cells with open-circuit voltage breaking the 1 V barrier. *Nat. Energy* **1**, 16015 (2016).
5. Zhao, Y. et al. Monocrystalline CdTe solar cells with open-circuit voltage over 1 V and efficiency of 17%. *Nat. Energy* **1**, 16067 (2016).
6. Metzger, W. K. et al. Exceeding 20% efficiency with in situ group V doping in polycrystalline CdTe solar cells. *Nat. Energy* **4**, 837 (2019).
7. Onno, A. et al. Understanding what limits the voltage of polycrystalline CdSeTe solar cells. *Nat. Energy* **7**, 400 (2022).
8. Fiducia, T. A. M. et al. Understanding the role of selenium in defect passivation for highly efficient selenium-alloyed cadmium telluride solar cells. *Nat. Energy* **4**, 504 (2019).
9. Kuciauskas, D., Moseley, J. & Lee, C. Identification of recombination losses in CdSe/CdTe solar cells from spectroscopic and microscopic time-resolved photoluminescence. *Sol. RRL* **5**, 2000775 (2021).
10. Kuciauskas, D. et al. Band bending at CdTe solar cell contacts: correlating electro-optical and X-Ray photoelectron spectroscopy analyses of thin film solar cells. *Sol. RRL* **7**, 2300073 (2023).
11. Kujovic, L. et al. Achieving 21.4% efficient CdSeTe/CdTe solar cells using highly resistive intrinsic ZnO buffer layers. *Adv. Funct. Mater.* **34**, 2312528 (2024).
12. Sartor, B. E. et al. Selective isolation of surface grain boundaries by oxide dielectrics improves Cd(Se,Te) device performance. *ACS Appl. Mater. Interfaces* **17**, 7641 (2025).
13. Ščajev, P. et al. As-doped polycrystalline CdSeTe: localized defects, carrier mobility and lifetimes, and impact on high-efficiency solar cells. *Adv. Energy Mater.* **15**, 2403902 (2025).
14. Kuciauskas, D. et al. Why increased CdSeTe charge carrier lifetimes and radiative efficiencies did not result in voltage boost for CdTe solar cells. *Adv. Energy Mater.* **13**, 2301784 (2023).
15. Rosenblatt, N., Hack, J., Lee, C., Zhang, Y.-H. & Metzger, W. K. Impacts of band edge fluctuations on CdSeTe solar cell performance and models. *APL Mater.* **12**, 111117 (2024).
16. Moseley, J. et al. Impact of dopant-induced optoelectronic tails on open-circuit voltage in arsenic-doped Cd(Se)Te solar cells. *J. Appl. Phys.* **128**, 103105 (2020).
17. McGott, D. L. et al. Investigation of sub-bandgap emission and unexpected n-type behavior in undoped polycrystalline CdSe$_x$Te$_{1-x}$. *Adv. Sci.* **11**, 2309264 (2024).
18. Jundt, P. et al. Photoluminescence investigations of CdSeTe absorbers to determine how selenium concentration influences attainable voltages, In *2024 IEEE 52nd Photovoltaic Specialist Conference (PVSC)* 692–696 (IEEE, Seattle, WA, USA, 2024).
19. Xiang, X., Tong, Y., Gehrke, A. & Dunham, S. T. Point defects in CdTe and CdTeSe alloy: a first principles investigation with DFT + U. *Phys. Rev. Mater.* **8**, 084602 (2024).

20. Xue, J. et al. Improved carrier lifetimes of CdSe thin film via Te doping for photovoltaic application. *ACS Appl. Mater. Interfaces* **15**, 17858–17866 (2023).

21. Xiang, X., Gehrke, A., Tong, Y. & Dunham, S. T. Multiscale modeling and optimization of group V doping and compensation in CdSe$_x$Te$_{1-x}$. *ACS Appl. Energy Mater.* **8**, 1248 (2025).

22. Hu, G. et al. Ultrafast photocarrier dynamics of CdSe$_x$Te$_{1-x}$ polycrystalline films under low illumination. *Sol. Energy* **258**, 289–293 (2023).

23. Myneni, S., Shaw, D., Munshi, A., Sampath, W. Sub-band gap emission in CdSe$_x$Te$_{1-x}$ devices by various post-deposition methods, In *2024 IEEE 52nd Photovoltaic Specialist Conference (PVSC)* 0887–0889 (IEEE, Seattle, WA, USA, 2024).

24. Frouin, B. et al. Quantitative assessment of selenium diffusion and passivation in CdSeTe solar cells probed by spatially resolved cathodoluminescence. *APL Mater.* **12**, 031135 (2024).

25. Krasikov, D. et al. Understanding ERE and iV$_{OC}$ metrics for graded CdSeTe absorbers. *Prog. Photovoltaics Res. Appl.* https://doi.org/10.1002/pip.3922 (2025).

26. Kuciauskas, D. et al. Voltage loss comparison in CdSe/CdTe solar cells and polycrystalline CdSeTe heterostructures. *IEEE J. Photovolt.* **12**, 6 (2022).

27. Scarpulla, M. A. et al. CdTe-based thin film photovoltaics: Recent advances, current challenges and future prospects. *Sol. Energy Mater. Sol. Cells* **255**, 112289 (2023).

28. Krasikov, D., Guo, D., Demtsu, S. & Sankin, I. Comparative study of As and Cu doping stability in CdSeTe absorbers. *Sol. Energy Mat. Sol. Cells* **224**, 111012 (2021).

29. McCandless, B. E. et al. Overcoming carrier concentration limits in polycrystalline CdTe thin films with In situ doping. *Sci. Rep.* **8**, 14519 (2018).

30. Jiang, C.-S. et al. Microelectronic structure and doping non-uniformity of phosphorus-doped CdSeTe solar cells. *ACS Appl. Mater. Interfaces* **17**, 3278–3288 (2025).

31. Neupane, S. et al. Ex situ bismuth doping for efficient CdSeTe thin-film solar cells with open-circuit voltages exceeding 900 mV. *Joule* **9**, 101766 (2025).

32. Kanevce, A., Reese, M. O., Barnes, T. M., Jensen, S. A. & Metzger, W. K. The roles of carrier concentration and interface, bulk, and grain-boundary recombination for 25% efficient CdTe solar cells. *J. Appl. Phys.* **121**, 214506 (2017).

33. Nagaoka, A., Kuciauskas, D. & Scarpulla, M. A. Doping properties of cadmium-rich arsenic-doped CdTe single crystals: Evidence of metastable AX behavior. *Appl. Phys. Lett.* **111**, 232103 (2017).

34. Krustok, J., Collan, H. & Hjelt, K. The low-temperature Arrhenius plot of the photoluminescence intensity in CdTe point towards an erroneous activation energy?. *J. Appl. Phys.* **81**, 1442 (1997).

35. Lee, D., Mysyrowicz, A., Nurmikko, A. V. & Fitzpatrick, B. J. Exciton self-trapping in ZnSe-ZnTe alloys. *Phys. Rev. Lett.* **58**, 1475 (1987).

36. Brasil, M. J. S., Motisuke, P., Decker, F. & Moro, J. R. Infrared photoluminescence at deep centres in polycrystalline CdSe layers. *J. Phys. C Solid State Phys.* **21**, 3141 (1988).

37. Kuciauskas, D. et al. Increased voltage in CdSe solar cells by mitigation of charge carrier trapping due to Se vacancies, in preparation.

38. Wright, A. D. et al. Electron–phonon coupling in hybrid lead halide perovskites. *Nat. Commun.* **7**, 11755 (2016).

39. Malikova, L. et al. Temperature dependence of the direct gaps of ZnSe and Zn$_{0.56}$Cd$_{0.44}$Se. *Phys. Rev. B* **54**, 1819 (1996).

40. Sweiti, A., Medina, F., Martinez, L. & Lopez-Rivera, A. Photoluminescence spectroscopy and effective concentration determination of Cd$_x$Zn$_{1-x}$Se. *Semicond. Sci. Technol.* **23**, 035019 (2008).

41. Moseley, J., Krasikov, D., Lee, C. & Kuciauskas, D. Diverse simulations of time-resolved photoluminescence in thin-film solar cells: A SnO$_2$/CdSe$_y$Te$_{1-y}$ case study. *J. Appl. Phys.* **130**, 163105 (2021).

42. Rosenwaks, Y., Tsimberova, I., Gero, H. & Molotskii, M. Minority-carrier recombination in p–InP single crystals. *Phys. Rev. B* **68**, 115210 (2003).

43. Perl, E. E., Kuciauskas, D., Simon, J., Friedman, D. J. & Steiner, M. A. Identification of the limiting factors for high-temperature GaAs, GaInP, and AlGaInP solar cells from device and carrier lifetime analysis. *J. Appl. Phys.* **122**, 233102 (2017).

44. Thomas, D. G., Hopfield, J. J. & Augustyniak, W. M. Kinetics of radiative recombination at randomly distributed donors and acceptors. *Phys. Rev.* **140**, A202 (1965).

45. Zacks, E. & Halperin, A. Dependence of the peak energy of the pair-photoluminescence band on excitation intensity. *Phys. Rev. B* **6**, 3072 (1972).

46. Wong, J., Omelchenko, S. T. & Atwater, H. A. Impact of semiconductor band tails and band filling on photovoltaic efficiency limits. *ACS Energy Lett.* **6**, 52 (2021).

47. Wolter, M. H. et al. How band tail recombination influences the open-circuit voltage of solar cells. *Prog. Photovoltaics: Res. Appl.* **30**, 702 (2022).

48. Ye, J. Y. et al. In situ formation of pseudohalide anions induced by humid air and light passivates formamidinium-based halide perovskites. *InfoMat* **7**, e12643 (2024).

49. Rau, U. & Werner, J. H. Radiative efficiency limits of solar cells with lateral band-gap fluctuations. *Appl. Phys. Lett.* **84**, 3735 (2004).

50. Yang, J. & Wei, S.-H. First-principles study of the band gap tuning and doping control in CdSe$_x$Te$_{1-x}$ alloy for high efficiency solar cell. *Chin. Phys. B* **28**, 086106 (2019).

51. Shklovskii, B. I., Efros, A. L. *Electronic Properties of Doped Semiconductors* (Springer Science & Business Media, 2013).

52. Ablekim, T. et al. Self-compensation in arsenic doping of CdTe. *Sci. Rep.* **7**, 4563 (2017).

53. Chatratin, I., Dou, B., Wei, S.-H. & Janotti, A. Doping limits of phosphorus, arsenic, and antimony in CdTe. *J. Phys. Chem. Lett.* **14**, 273 (2023).

54. Swartz, C. H. et al. Factors influencing photoluminescence and photocarrier lifetime in CdSeTe/CdMgTe double heterostructures. *J. Appl. Phys.* **120**, 165305 (2016).

55. Ščajev, P. et al. Excitation-dependent carrier lifetime and diffusion length in bulk CdTe determined by time-resolved optical pump-probe techniques. *J. Appl. Phys.* **123**, 025704 (2018).

56. Ščajev, P. et al. Impact of dopant-induced band tails on optical spectra, charge carrier transport, and dynamics in single-crystal CdTe. *Sci. Rep.* **12**, 12851 (2022).

57. Kober-Czerny, M. et al. Determining parameters of metal-halide perovskites using photoluminescence with Bayesian inference, PRX. *Energy* **4**, 013001 (2025).

58. Abou-Ras, D. Microscopic origins of radiative performance losses in thin-film solar cells at the example of (Ag,Cu)(In,Ga)Se$_2$ devices. *J. Vac. Sci. Technol. A* **42**, 022803 (2024).

59. Gloeckler, M., Fahrenbruch, A. L., Sites, J. R. Numerical modeling of CIGS and CdTe solar cells: setting the baseline. In *Photovoltaic Energy Conversion, Proceedings of 3rd World Conference on* 491–494 (IEEE, Osaka, Japan, 2003).

60. Gokmen, T., Gunawan, O. & Mitzi, D. B. Semi-empirical device model for Cu$_2$ZnSn(S,Se)$_4$ solar cells. *Appl. Phys. Lett.* **105**, 033903 (2014).

61. Moore, J. E., Hages, C. J., Agrawal, R., Lundstrom, M. S. & Gray, J. L. The importance of band tail recombination on current collection and open-circuit voltage in CZTSSe solar cells. *Appl. Phys. Lett.* **109**, 021102 (2016).

62. Nardone, M. et al. Comprehensive model for evaluating voltage losses and performance improvements in thin-film photovoltaic devices. *Phys. Rev. Appl.* **23**, 034019 (2025).

63. Rühle, S. Tabulated values of the Shockley–Queisser limit for single junction solar cells. *Sol. Energy* **130**, 139–147 (2016).

64. Marti, A., Balenzategui, J. L. & Reyna, R. F. Photon recycling and Shockley's diode equation. *J. Appl. Phys.* **82**, 4067 (1997).

65. Kim, S. H. et al. Extremely suppressed energetic disorder in a chemically doped conjugated polymer. *Adv. Mater.* **35**, 2207320 (2023).

66. Kuciauskas, D., Moseley, J., Ščajev, P. & Albin, D. Radiative efficiency and charge-carrier lifetimes and diffusion length in polycrystalline CdSeTe heterostructures. *Phys. Status Solidi RRL* **14**, 1900606 (2020).

Author contributions

Conceptualization and methodology: D.K., M.N., P.Š., C.-S. J., D.L., R.F.; investigation: D.K., M.N., P.Š., C.-S. J., R.F.; writing-original draft preparation: D.K., M.N.; writing-review and editing: D.K., M.N., P.Š., C.-S. J., D.L., R.F.; funding acquisition: D.K. and M.N. All authors have read and agreed to the published version of the manuscript.

Competing interests

The authors declare no competing interests.

Additional information

Supplementary information The online version contains supplementary material available at https://doi.org/10.1038/s41467-025-63589-7.

Correspondence and requests for materials should be addressed to Darius Kuciauskas.

Peer review information *Nature Communications* thanks Michael Scarpulla, and the other, anonymous, reviewer(s) for their contribution to the peer review of this work. A peer review file is available.

Reprints and permissions information is available at http://www.nature.com/reprints

Publisher's note Springer Nature remains neutral with regard to jurisdictional claims in published maps and institutional affiliations.